

Synthesis and characterization of novel porous $\text{La}_2\text{Zr}_2\text{O}_7$ ceramic with ultralow thermal conductivity and excellent photocatalytic property

Baosehng Xu (✉ xubsh@bit.edu.cn)

Beijing Institute of Technology

Debao LIU

Beijing Institute of Technology

Liyan GENG

Shanghai Institute of Space Power-Sources

Feifei ZHOU

Beijing Institute of Technology

Lijie QU

Beijing Institute of Technology

Yiguang WANG

Beijing Institute of Technology

Baosheng XU

Beijing Institute of Technology

Shigang AI

Beijing Institute of Technology

Research Article

Keywords: $\text{La}_2\text{Zr}_2\text{O}_7$, porous ceramic, sol-gel template method, thermal conductivity, photocatalytic

Posted Date: August 25th, 2021

DOI: <https://doi.org/10.21203/rs.3.rs-820717/v1>

License: © ⓘ This work is licensed under a Creative Commons Attribution 4.0 International License.

[Read Full License](#)

Abstract

A novel porous $\text{La}_2\text{Zr}_2\text{O}_7$ ceramic prepared by combining a sol-gel template method and high-temperature calcination process. The structural evolution and crystallisation behaviour of the samples were systematically characterized using SEM, XRD, TEM and Raman spectroscopy. The results indicated that the as-prepared porous $\text{La}_2\text{Zr}_2\text{O}_7$ ceramic had a typical nanoparticles assembling and mesoporous structure with single-phase pyrochlore crystal structure. Meanwhile, the as-prepared porous $\text{La}_2\text{Zr}_2\text{O}_7$ ceramic presented an ultralow room temperature thermal conductivity of $0.07 \text{ W}/(\text{m}\cdot\text{K})$, high specific surface areas of $325.17 \text{ m}^2/\text{g}$ and a relatively high compressive strength of 11.95 MPa . What's more, the as-prepared porous $\text{La}_2\text{Zr}_2\text{O}_7$ ceramic possessed ideal photocatalytic activity owing to the unique 3-D porous structure, high crystallinity and large surface area. These reported studies are proposing some new insight to improve porous rare-earth zirconates ceramic for thermal insulation and dye degradation applications.

1. Introduction

Lanthanum zirconate ($\text{La}_2\text{Zr}_2\text{O}_7$) belongs to a family of compounds with the general formula $\text{A}_2\text{B}_2\text{O}_7$, where A denotes trivalent rare earth elements and B a tetravalent cation, which has a face-centered cubic crystal structure with the space group $Fd3m$ (No. 227) [1, 2]. Some outstanding properties for $\text{La}_2\text{Zr}_2\text{O}_7$ are performed, such as high melting point, low thermal conductivity, high thermal expansion coefficient, excellent thermal stability, and high tolerance to defects [3–6]. Those properties are attributable to the pyrochlore crystal structures that is a superstructure derivative of the simple fluorite. As such, $\text{La}_2\text{Zr}_2\text{O}_7$ has attracted significant interest in various applications, such as high temperature ceramic thermal barrier coating materials, photocatalysts, solid electrolytes, nuclear waste containers, host materials for luminescence centers and so on [7–11].

In order to improve the properties of the $\text{La}_2\text{Zr}_2\text{O}_7$ and broaden the fields of its application, the preparation methods of $\text{La}_2\text{Zr}_2\text{O}_7$ have been received considerable attention especially in recent years, including the conventional solid-state mixing method [12, 13], hydrothermal synthesis [14], coprecipitation route [15, 16], combustion synthesis [17], molten salt method [18, 19], sol-gel method [20, 21], and hydrazine method [22]. However, of these methods, the synthesis of $\text{La}_2\text{Zr}_2\text{O}_7$ materials usually requires tedious process (long reaction times), harsh condition (high temperatures and pressures), environmental hazardous, etc. For example, solid-state reaction requires a reaction temperature above $1000 \text{ }^\circ\text{C}$ and a reaction time above 10 h [23], which is easy to cause agglomeration and instability of the nano/micro structure. Whereas, in the hydrothermal method, the surfactant is required to reduce the reaction time [24]. However, from the viewpoint of green chemistry, the aqueous surfactant mixture wastes produced from these processes are hazardous to the environment. Therefore, it is very necessary to develop a new efficient method with the advantages of simple operation, low energy consumption, low cost and no secondary pollution, which can endow $\text{La}_2\text{Zr}_2\text{O}_7$ with multifunctional properties.

Herein, in the present work, we demonstrated firstly the synthesis of a novel porous $\text{La}_2\text{Zr}_2\text{O}_7$ ceramic by combining a sol-gel template method and high-temperature calcination process. The micro-structural, room-temperature thermal conductivity property, mechanical properties as well as photocatalytic activities of porous $\text{La}_2\text{Zr}_2\text{O}_7$ ceramic aerogels were systematically studied. In addition, the surface area of this materials is high after heat treatment. This synthetic strategy was performed to develop a new preparation method of porous $\text{La}_2\text{Zr}_2\text{O}_7$ ceramic and can be extended for the preparation of other porous ceramic materials with multifunctional properties.

2. Experimental Procedures

2.1 Materials

Commercially available thermoplastic phenolic resin (RF; 99.9%, Shandong Shengquan Chem Co., Ltd., China), urotropine (AR, 99.0%, Guangdong Xilong Chem Co., Ltd., China) and anhydrous ethanol (AR, Tianjin Fuchen Chem Co., Ltd., China) were used as a sacrifice template, a curing agent and a solvent, respectively. $\text{La}(\text{NO}_3)_3 \cdot 6\text{H}_2\text{O}$ (AR, > 99.9%, Shanghai Macklin Biochemical Co., Ltd., China) and $\text{Zr}(\text{CH}_3\text{COO})_4$ (Zr, 15.0–16.0%, Shanghai Aladdin Biochemical Co., Ltd., China) were used as raw materials. Methylene blue (MB) dye chemical was used for photocatalytic study.

2.2 Preparation of the samples

To begin our optimization studies for the synthesis of porous $\text{La}_2\text{Zr}_2\text{O}_7$ ceramic powders and bulks. The fabrication procedure was illustrated in Scheme. 1. Firstly, 0.45 g RF was dissolved in 10 mL ethanol and stirred for 1 h to obtain a clear RF sol. Afterwards, 0.151 g (1 mmol) $\text{Zr}(\text{CH}_3\text{COO})_4$, 0.433 g (1 mmol) $\text{La}(\text{NO}_3)_3 \cdot 6\text{H}_2\text{O}$ and 0.8 g urotropine were added and stirred for another 1 h. A homogeneous mixture solution (M/RF sol) was then introduced to a stainless-steel Teflon lined autoclave, kept at 80 °C for 20 h and naturally cooled to room temperature. The obtained wet gel (M/RF gel) was placed in ethanol for solvent exchange and aging. Then the ethanol was replaced every 6 h for 4 times. Subsequently, the La^{3+} and Zr^{4+} -doped RF aerogel (M/RF aerogel) was prepared via an ethanol supercritical drying process (SCD). Finally, the porous $\text{La}_2\text{Zr}_2\text{O}_7$ ceramic was obtained after thermal treated at 1000 °C–1200 °C in air for 2 h (2 °C/min). To facilitate the presentation next, the sample of $\text{La}_2\text{Zr}_2\text{O}_7$ calcined at 1000 °C, 1100 °C and 1200 °C are named as LZ1, LZ2 and LZ3, respectively.

In order to obtain the bulks, for example, the as-synthesized LZ1 powders were mixed with proper amount of polyvinyl alcohol (PVA) binder for granulation. After that, the mixed powders were ground and sifted through a 80-mesh sieve, and then pressed into cylindrical disks at a uniaxial pressure of 50 MPa for 2 min, while the size of the bulks can be adjusted according to the actual testing requirements. Finally, the compressed disks were calcined at 600 °C for 2 h (1 °C/min, in air) to burn out the PVA binders. Other bulk samples were also prepared under the same conditions and named as LZ2 bulk and LZ3 bulk.

2.3 Materials characterization

High-resolution images of the samples were obtained by FESEM (JSM-7800 F, JEOL) at an acceleration voltage of 15 kV. Energy dispersive X-ray spectroscopy (EDX, X-Max SDD Detector, Oxford Instruments) was employed to identify the elements present in the products. Transmission electron microscopy (TEM, Talos F200X G2, US) with EDS and selected-area electron diffraction (SAED) were conducted to analyse the morphological characteristics and crystalline structure of the obtained samples. X-ray diffraction (XRD) measurement was performed using a diffractometer (XRD diffractometer Bruker AXS D8) with Cu K_{α} radiation ($\lambda = 1.54 \text{ \AA}$) in a 2θ range of 20° – 90° with a scanning rate of $5^{\circ}/\text{min}$. High-resolution Raman spectrometer (Renishaw, RM2000, UK) was carried out to analyse Raman spectra. The Fourier transform infrared spectrum (FT-IR) were recorded on a WQF-410 spectro- photometer (Beijing Secondary Optical Instruments, China). The surface areas of sample were characterized by Brunauer-Emmett-Teller (BET) principle and porous structures of products were determined by Barrett-Joyner-Halenda (BJH) method using Nitrogen adsorption- desorption measurements (MFA-140, Beijing Builder Company, China).

2.4 Measurements of thermal conductivity and mechanical property

The as-synthesized $\text{La}_2\text{Zr}_2\text{O}_7$ cylindrical pellets with standard size ($\Phi = 50 \text{ mm}$; $d = 5 \text{ mm}$) were used to conduct the room-temperature thermal conductivity measurements by using a thermal conductivity instrument (DRE-III, Xiangtan Xiangyi Instrument Co., Ltd., Xiangtan, China). The $\text{La}_2\text{Zr}_2\text{O}_7$ samples ($\Phi = 22 \text{ mm}$; $d = 10 \text{ mm}$) were loaded at a testing machine (Instron 5569, Instron corp., Canton, USA) to test the compressive strength, with a crosshead speed of $0.05 \text{ mm}/\text{min}$. The samples were machined with the compressive surface perpendicular to the freezing direction. In order to obtain the average value, more than 6 samples of each measurement were chosen.

2.5 The photocatalytic property

The photocatalytic property of the samples were evaluated by rhodamine B (RhB) decomposition under UV-light. A commercial 250 W halogen spotlight (the spectrum below 400 nm removed using a cutoff filter) was used for the UV-light illumination. The initial concentration of RhB in quartz reaction vessel was fixed at $50 \text{ mg}/\text{L}$ with as-obtained catalyst loading of $1 \text{ g}/\text{L}$. Before irradiation, the solution was under magnetic stirring for 30 min to ensure the adsorption-desorption equilibrium. Then the solution was stirred and exposed to the UV-light irradiation. The extent of RhB decomposition was determined by measuring the absorbance value at 465 nm using UV-1201 spectrometer. Emission/excitation spectra were recorded on a Hitachi F-4500 fluorescence spectrophotometer at room temperature.

3. Results And Discussion

Figure 1(a) showed the XRD ($5^{\circ}/\text{min}$) patterns of the as-prepared LZ1. No characteristic reflections of impurities were detected, demonstrated a face-centered cubic pure pyrochlore type structure (JCPDS No. 01-071-2363). Notably, the peaks marked with black peach for the LZ1 were characteristic superlattice diffraction peaks of pyrochlore structure [25].

The Raman spectra of the LZ1 were presented in Fig. 1(b). According to symmetry theory, the Raman spectra are very sensitive to the vibrations of the O cation. The pyrochlore structure usually consists of six Raman active vibration modes as follows:

$$\Gamma(\text{Raman}) = A_{1g} + E_g + 4F_{2g} . \quad (1)$$

For an ideal pyrochlore structure, the six vibration modes are associated with an O cation, including one mode (F_{2g}) related to the O cation at the 8a site and five modes ($A_{1g} + E_g + 3F_{2g}$) assigned to the O cation at the 48f site, where E_g is derived from the O-RE-O bending vibrations [26, 27]. The LZ1 presented four typical vibration modes in the range of 200–800 cm^{-1} without other vibration modes, indicating a pyrochlore structure.

The simulated model of an ideal crystal structure diagram of pyrochlore was depicted in Fig. 1(c). An ideal pyrochlore structure belongs to the space group $Fd\bar{3}m$ ($Z = 8$), where La^{3+} distributed randomly and equally at the 16c site, and the Zr^{4+} equally and homogeneously occupy the 16d site. The O occupies the 8b and 48f sites, while the O vacancy occupies the 8a site [28].

The FT-IR spectra of LZ1 in the wave range of 400 cm^{-1} to 4000 cm^{-1} were presented in Fig. 1(d). The peaks centered approximately at 1187 cm^{-1} and 1108 cm^{-1} are ascribed to the stretching vibration of Zr atoms against O atoms in Zr-O-Zr bond [29]. While the peaks at the vicinity of 540 cm^{-1} and 3690 cm^{-1} are correspond to the vibration of the chemical bond Zr-O stretching modes. A relatively weak band centered at about 436 cm^{-1} associated with the vibration of O-La-O bending modes [30]. Also, the appearances of the band centered at approximately 1630 cm^{-1} are evidence of the existence of water molecules attached to the powders.

Figure 2(a, b) depicted the SEM and TEM images of the calcined LZ1. Clearly, the samples have a good microstructural integrity with a typical “pearl chain” microstructure, which presented a 3-D porous network skeleton with numerous nanoscale particles and nanopores. The nanoscale particles (approximately 25–35 nm) were uniformly distribute in the whole field of vision with an average particle size. The nanopores presented open and close pore structures with an average size of approximately 40–50 nm. HRTEM was performed to further verify the information of the LZ1 with pyrochlore structure (Fig. 2(c)). The observed interplanar spacing of 0.182 nm and 0.173 nm were corresponded to the (222) and (440) planes, respectively. The SAED pattern of LZ1 were shown in Fig. 2(d). The Miller indices (hkl) of all the crystal planes of LZ1 obtained from SAED pattern are in good agreement with XRD reference patterns. The LZ1 were further examined through EDS mapping to investigate the element distribution homogeneity on the nanoscale, as shown in Fig. 2(e), all the elements contained were uniformly distributed without any noticeable elemental segregation or clustering.

Figure 3 showed the microstructures and the corresponding XRD patterns of the $\text{La}_2\text{Zr}_2\text{O}_7$ powders calcined at different temperature. It can be seen from Fig. 3(a) that the enlarged particles and decreased

size of pores. Nevertheless, the 3-D porous network skeleton of the microstructure still present. As for sample LZ3 (Fig. 3(b)), we can clearly see that the particles were grow bigger in the whole field of view and many of them seemed closely combined. The pores still exist though most of them disappeared and the interconnected assembly forms a relatively dense structure. The corresponding XRD patterns of three samples calcined at different temperatures were shown in Fig. 3(c). Obviously, the three samples presented a single-phase pyrochlore structure without other phases. However, because of the lattice constant increase, the diffraction peak positions slightly shifted toward a lower diffraction angle as the calcined temperatures increase [31].

Figure 4 showed the N₂ adsorption-desorption isotherms and corresponding BJH pore size distribution analysis of the samples. It appeared a typical type IV adsorption isotherm with an H3-type hysteresis loop in accordance with mesoporous structure [32]. The BET specific surface areas were calculated to be 325.17, 221.43 and 62.57 m²/g for samples LZ1, LZ2 and LZ3, respectively. The pore size distribution curve (inset images) depicted that the samples exhibited mesopore and macropore size regions with a small average pore width and a high pore volume. The BET specific surface area of the samples decreased because the grains further grow. Simultaneous, the pore size of the samples decreased as the calcination temperature increases.

Figure 5(a) depicted the photograph of the as-prepared LZ1 bulk reconstructed under a uniaxial pressure of 50 MPa, which shows an intact overall structure. The surface morphology with low magnification which demonstrated a uniform, regular and dense morphology, as shown in Fig. 5(b). The magnified surface morphology (Fig. 5(c)) showed a 3-D porous network skeleton with no structural destroyed.

The room temperature thermal conductivity of the samples were shown in Fig. 6(a). Clearly, the room-temperature thermal conductivity were 0.07 W/(m·K), 0.09 W/(m·K) and 0.13 W/(m·K) for the sample LZ1, LZ2 and LZ3 bulk, respectively. The lower room temperature thermal conductivity can attributed to the unique 3-D interconnected porous structures with rich porosity, and the ceramics grains were not continuous that can block the heat conducting pathways [33]. We can conclude that the high porosity can greatly reduce the effective thermal conductivity of the porous La₂Zr₂O₇ bulk. What's more, combining with the results of Fig. 4, the specific surface area (SSA) is another factor for decreasing thermal conductivity of porous La₂Zr₂O₇ bulk. For a given density, the smaller the size of the pores, the higher the SSA, and the better will be the insulation performance.

The heat conductivity mechanisms within aerogels were systematically sketched out in Fig. 6(b). Heat transfer in monolithic non-evacuated aerogels involves three components, since the convection heat transfer can be neglected in porous materials where void spaces are smaller than 4 mm. Thus, the total thermal conductivity can be described as follows [34].

$$k_T = k_s + k_g + k_r \quad (2)$$

where k_T is the total thermal conductivity and k_s , k_g , and k_r refer, respectively, to the solid, gaseous and radiative transfer components of the first.

The k_s relates to the solid fraction of aerogels which is influenced by the extent of crosslinking and network connectivity. Heat conduction in the solid network occurs through the atomic lattice, due to the excitation of vibrational energy levels of interatomic bonds or even by free electron transport under thermal gradient [35]. When the heat conducted in the gaseous state, the collision phenomenon happens and the faster ones transfer part of their kinetic energy to the slower molecules. But the movements are of minor relevance in the monolithic native aerogels because the average pore dimensions are typically below 70 nm, and the mean free path of air molecules is about 66 nm [36]. The k_r is based on electromagnetic waves, correlated to the photon's mean free path. Therefore, this component is highly temperature-dependent, with a high factor-scaling exponent. According to Fomitchev [37], the radiative thermal conductivity can be computed as follows:

$$K_r = 16n^2\sigma T^3\varepsilon^{-1} \quad (3)$$

where n is the index of refraction, σ is the Stefan-Boltzmann constant, T is the temperature (K) and ε ($\varepsilon = \rho_b e$) is the spectral attenuation coefficient.

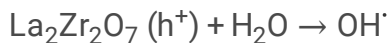
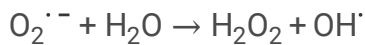
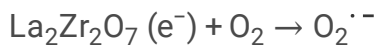
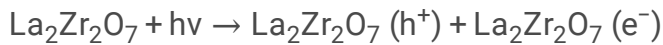
In conclusion, the extremely low thermal conductivity of the as-prepared porous $\text{La}_2\text{Zr}_2\text{O}_7$ bulks were result from the combination effect of the three heat conduction modes.

The pore structure and morphology of the particles also have a significant effect on the mechanical properties of porous $\text{La}_2\text{Zr}_2\text{O}_7$ ceramic. Figure 7 depicted that the compressive strength values were 5.22, 8.34 and 11.95 MPa for sample LZ1, LZ2 and LZ3 bulk, respectively. Even though the compressive strength values here were lower compared with reported work [38], the as-prepared porous $\text{La}_2\text{Zr}_2\text{O}_7$ ceramic in this work had much higher porosity. According to Griffith theory, the critical crack size has a vital effect on the mechanical strength and the cracks are mainly result from the pores. Since the stress concentrates on the surrounding region of pores, and the pores can decrease the load area and weaken the load capability [39]. The porosity decreased with the increasing of sintering temperature and the interconnected adjacent particles formed a strong neck, which enhancing the compressive strength.

The LZ1 bulk samples were utilized as photocatalyst for the photo-degradation of RhB dye. As depicted in Fig. 8(a), different absorption spectrums of RhB solution taken out at different times were characterized by UV-light irradiation. At the initial stage, the spectrum showed the maximum absorption peaks of RhB at 553 nm. The absorption peak intensity decreased with prolonging irradiation time, demonstrating the gradual degradation of the organic dye. The inset showed the photograph of RhB solution at beginning and after 60 min of UV-light exposure. The color of the solution was almost faded away, manifesting the degradation of the dye molecules. The characterization of degradation efficiencies of the three photocatalysts were presented in Fig. 8(b). It is the plot of degradation C/C_0 as a function of irradiation time, where C is the absorbance of RhB solution measured every 10 min in the process of

photodegradation and C_0 is the original RhB solution. It was clear that the degradation efficiencies of the LZ1 photocatalyst was ideal and the dye is decomposed 73% after UV-light treated for 60 min, demonstrating a better photocatalytic degradation performance than its counterparts. Figure 8(c) depicted the re-use performances of LZ1 photocatalyst. Though the photocatalytic degradation under UV-light irradiation has a little changed, the yield was still 60% after repeating 4 times. The enhanced photocatalytic performance of LZ1 photocatalyst can ascribed to its unique 3-D porous structure and high specific surface area, which provided more electrons-holes (h^+e^-) that facilitating the enhancement for photocatalytic properties.

The $La_2Zr_2O_7$ photocatalyst has received significant attention due to the absorption of oxygen (O_2) and water molecules (H_2O) on the porous structures surface of the photocatalyst by the effect of UV light irradiation [40]. In order to explore the photocatalytic mechanism, the band energy levels of $La_2Zr_2O_7$ samples were depicted in Fig. 8(d). When exposed to UV light, the $La_2Zr_2O_7$ absorbed photon of energy greater than the energy band gap (E_g) electrons (e^-) and excited from valence band (VB) into the vacant conduction band (CB). Based on the reports [41, 42], a possible mechanistic pathway of the $La_2Zr_2O_7$ catalyst is shown as follows:



The electrons (e^-) at CB of $La_2Zr_2O_7$ were scavenged by dissolved O_2 and produce superoxide radicals ($O_2^{\cdot -}$), and the produced $O_2^{\cdot -}$ then reacts with H_2O to form hydroxyl radicals (OH^{\cdot}). Also, the holes (h^+) in VB of $La_2Zr_2O_7$ can react with H_2O and generate OH^{\cdot} . The produced OH^{\cdot} can decompose the RhB organic dye molecule into the smaller organic molecules [43], H_2O , CO_2 , and mineral acids.

4. Conclusions

In this study, a novel porous $La_2Zr_2O_7$ ceramic was successfully fabricated by combining a sol-gel template method and high-temperature calcination process. The micro-structural, room temperature thermal conductivity property, mechanical properties as well as photocatalytic activities of the samples were systematically studied. The as-prepared porous $La_2Zr_2O_7$ ceramic exhibited an ultralow room-temperature thermal conductivity, high specific surface areas, relatively high compressive strength, and ideal photocatalytic activities. The combining of sol-gel template method and high-temperature

calcination process can be considered as an efficient technique to prepare porous rare-earth zirconates ceramic materials with multifunctional properties for applications in the fields of thermal insulators and dye degradation applications.

Declarations

Competing Interest

The authors declare that they have no known competing financial interests or personal relationships that could have appeared to influence the work reported in this paper.

Acknowledgements

This work is supported by the Beijing Institute of Technology Research Fund Program for Young Scholars, National Science and Technology Major Project (2017-VI-0020-0093) and National Natural Science Foundation of China (Nos.12090031 and 11602125).

References

1. Subramanian MA, Aravamudan G, Subba Rao GV et al (1983) Oxide pyrochlores—A review. *Prog Solid State Chem* 15:55–143
2. Liu ZG, Hu KJ, Jin YJ et al (2015) Preparation and photoluminescence properties of Er³⁺-doped La₂Zr₂O₇ nanocrystals. *J Alloys Compounds* 653:122–125
3. Modeshia DR, Walton RI (2010) Solvothermal synthesis of perovskites and pyrochlores: crystallisation of functional oxides under mild conditions. *Chem Soc Rev* 39:4303–4325
4. Vassen R, Cao XQ, Tietz F et al (2000) Chem Inform Abstract: Zirconates as New Materials for Thermal Barrier Coatings. *J Am Ceram Soc* 83:2023–2028
5. Sickafus KE, Minervini L, Grimes RW et al (2000) Radiation Tolerance of Complex Oxides. *Science* 289:748–751
6. Cao XQ, Vassen R, Jungen W et al (2001) Thermal Stability of Lanthanum Zirconate Plasma-Sprayed Coating. *J Am Ceram Soc* 84:2086–2090
7. Hu KJ, Liu ZG, Wang JY et al (2013) Influence of calcination temperature on synthesis and photoluminescence properties of Eu³⁺-doped La₂Zr₂O₇ particles. *J Alloys Compd* 576:177–180
8. Xu ZH, Zhou X, Wang K et al (2014) Thermal barrier coatings of new rare-earth composite oxide by EB-PVD. *J Alloys Compd* 587:126–132
9. Liu ZG, Ouyang JH, Sun KN et al (2014) Effect of metal oxides on the densification and electrical conductivity of the GdSmZr₂O₇ ceramic. *J Alloys Compd* 617:393–398
10. Tian JS, Peng HG, Xu XL et al (2015) High surface area La₂Sn₂O₇ pyrochlore as a novel, active and stable support for Pd for CO oxidation. *Catal Sci Technol* 5:2270–2281

11. Lu ZR, Fan L, Shu XY et al (2015) Phase evolution and chemical durability of co-doped $Gd_2Zr_2O_7$ ceramics for nuclear waste forms. *Ceram Int* 41:6344–6349
12. Harvey EJ, Whittle KR, Lumpkin GR et al (2005) Solid solubilities of $(La,Nd)_2(Zr,Ti)_2O_7$ phases deduced by neutron diffraction. *J Solid State Chem* 178:800–810
13. Digeos AA, Valdez JA, Sickafus KE et al (2003) Glass matrix/pyrochlore phase composites for nuclear wastes encapsulation. *J Mater Sci* 8:1597–1604
14. Chen D, Xu R (1998) Hydrothermal synthesis and characterization of $La_2M_2O_7$ powders. *Mater Res Bull* 33:409–417
15. Vassen R, Cao XQ, Tietz F et al (2000) Zirconates as new materials for thermal barrier coatings. *J Am Ceram Soc* 83:2023–2028
16. Chen H, Gao Y, Luo H et al (2011) Preparation and thermophysical properties of $La_2Zr_2O_7$ coatings by thermal spraying of an amorphous precursor. *J Therm Spray Technol* 20:1201–1208
17. Aruna ST, Sanjeeviraja C, Balaji N et al (2013) Properties of plasma sprayed $La_2Zr_2O_7$ coating fabricated from powder synthesized by a single-step solution combustion method. *Surf Coat Technol* 219:131–138
18. Mao Y, Guo X, Huang JY et al (2009) Luminescent nanocrystals with $A_2B_2O_7$ composition synthesized by a kinetically modified molten salt method. *J Phys Chem C* 113:1204–1208
19. Wang X, Zhu Y, Zhang W (2010) Preparation of lanthanum zirconate nano-powders by Molten Salts method. *J Non-Cryst Solids* 365:1049–1051
20. Kong L, Karatchevtseva I, Gregg DJ et al (2013) A novel chemical route to prepare $La_2Zr_2O_7$ pyrochlore. *J Am Ceram Soc* 96:935–941
21. Wang SX, Wei L, Wang S et al (2015) Synthesis of nanostructured $La_2Zr_2O_7$ by a non-alkoxide sol-gel method: From gel to crystalline powders. *J Eur Ceram Soc* 35:105–112
22. Matsumura Y, Yoshinaka M, Hirota K et al (1997) Formation and sintering of $La_2Zr_2O_7$ by the hydrazine method. *Solid State Commun* 104:341–345
23. Tong Y, Zhu J, Lu L et al (2008) Preparation and characterization of $La_2Zr_2O_7$ (Ln = La and Nd) nanocrystals and their photocatalytic properties. *J Alloys Comp* 465:280–284
24. Chen D, Xu R (1998) Hydrothermal synthesis and characterization of $La_2M_2O_7$ (M = Ti, Zr) powders. *Mater Res Bull* 33:409–417
25. Teng Z, Zhu LN, Tan YQ et al (2019) Synthesis and structures of high-entropy pyrochlore oxides. *J Eur Ceram Soc* 40:1639–1643
26. Wan CL, Qu ZX, Du AB et al (2011) Order-Disorder Transition and Unconventional Thermal Conductivities of the $(Sm_{1-x}Yb_x)_2Zr_2O_7$ Series. *J Am Ceram Soc* 94:592–596
27. Liu DB, Xu BS, Lv BV et al. A novel high-entropy $(Sm_{0.2}Eu_{0.2}Tb_{0.2}Dy_{0.2}Lu_{0.2})_2Zr_2O_7$ ceramic aerogel with ultralow thermal conductivity. *Ceram Inter* doi.org/10.1016/j.ceramint.2021.07.170

28. Vayer F, Decorse C, Bérardan D et al (2021) New entropy-stabilized oxide with pyrochlore structure: $\text{Dy}_2(\text{Ti}_{0.2}\text{Zr}_{0.2}\text{Hf}_{0.2}\text{Ge}_{0.2}\text{Sn}_{0.2})_2\text{O}_7$. *J Alloy Compd* 41:6080–6086
29. Diaz M, Pecharroman C, Monte FD et al (2005) Synthesis, thermal evolution, and luminescence properties of yttrium disilicate host matrix. *Chem Mater* 17:1774–1782
30. Zhou L, Huang ZY, Qi JQ et al (2016) Thermal-Driven Fluorite-Pyrochlore-Fluorite Phase Transitions of $\text{Gd}_2\text{Zr}_2\text{O}_7$ Ceramics Probed in Large Range of Sintering Temperature. *Metall Mater Trans A* 47:623–630
31. Ren K, Wang QK, Wang YG et al (2020) Multicomponent high-entropy zirconates with comprehensive properties for advanced thermal barrier coating. *Scrip Mater* 178:382–386
32. Rodríguez JT, Cano VG, Menelaou M et al (2019) Rare-Earth Zirconate $\text{Ln}_2\text{Zr}_2\text{O}_7$ (Ln: La, Nd, Gd, and Dy) Powders, Xerogels, and Aerogels: Preparation, Structure, and Properties. *Inorg Chem* 58:14467–14477
33. Zhang RB, Fang DN, Chen XM et al (2013) Microstructure and properties of highly porous Y_2SiO_5 ceramics produced by a new water-based freeze casting. *Mater Design* 46:746–750
34. Wei G, Liu Y, Zhang X et al (2011) Gaseous Conductivity Study on Silica Aerogel and Its Composite Insulation Materials. *Int J Heat Mass Transfer* 54:2355–2366
35. Duraes L, Maleki H, Vareda JP et al (2017) Exploring the Versatile Surface Chemistry of Silica Aerogels for Multipurpose Application. *MRS Adv* 2:3511–3519
36. Modest MF, Radiative Heat Transfer: Second Edition. *Academic Press San Diego* 2003
37. Linhares T, Pessoa MT, Amorim et al (2019) Silica aerogel composites with embedded fibres: a review on their preparation, properties and applications. *J Mater Chem A* 7:22768–22802
38. Sun ZQ, Li MS, Zhou YC (2009) Thermal properties of single-phase Y_2SiO_5 . *J Eur Ceram Soc* 29:551–557
39. Xia YF, Zeng YP, Jiang DL (2012) Microstructure and mechanical properties of porous Si_3N_4 ceramics prepared by freeze-casting. *Mater Des* 33:98–103
40. Kombaiah K, Vijaya JJ, Kennedy LJ et al (2017) Studies on opuntia dilenii haw mediated multifunctional ZnFe_2O_4 nanoparticles: optical, magnetic, and catalytic applications. *Mater Chem Phys* 194:153–164
41. Fu F, Chen Q, He M et al (2012) A multifunctional hetero architecture for photocatalysis and energy storage. *Ind Eng Chem Res* 51:11700–11709
42. Al-Ghouthi MA, Khraisheh MA, Allen SJ et al (2003) The removal of dyes from textile wastewater: a study of the physical characteristics and adsorption mechanisms of diatomaceous earth. *J Environ Managm* 69:229–238
43. Chen MZ, Jia YM, Li HM et al (2021) Enhanced photocatalysis of the pyroelectric $\text{BiFeO}_3/\text{g-C}_3\text{N}_4$ heterostructure for dye decomposition driven by cold-hot temperature alternation. *J Adv Ceram* 10(2):338–346

Figures

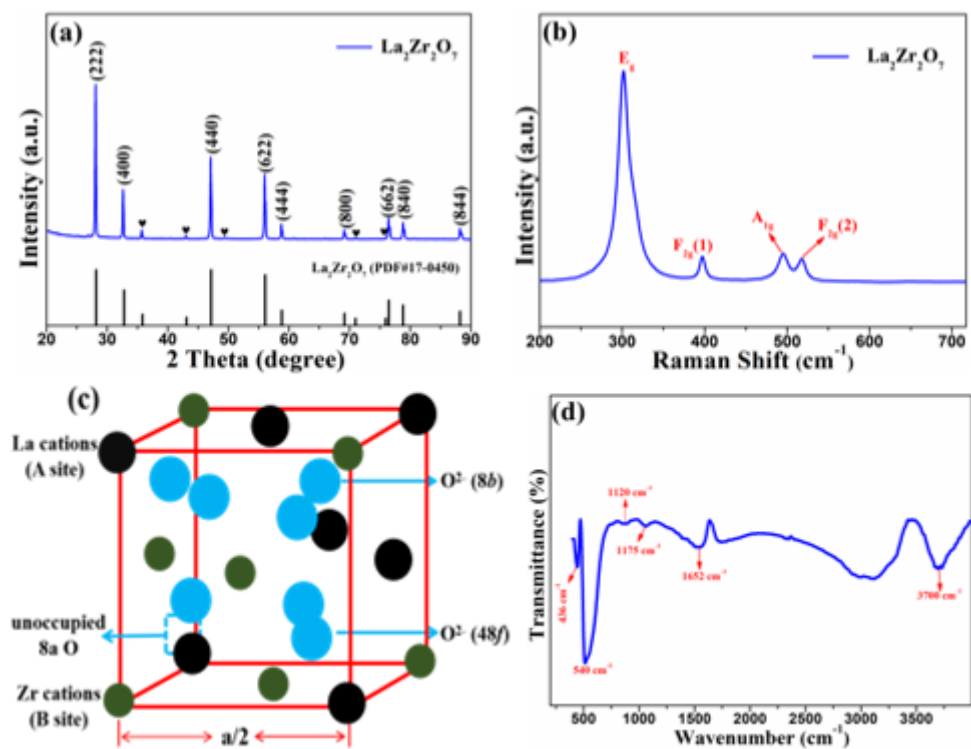


Figure 1

(a) The X-ray diffraction pattern. (b) Raman spectrum. (c) the crystal structure schematic and (d) the FT-IR spectra of LZ1.

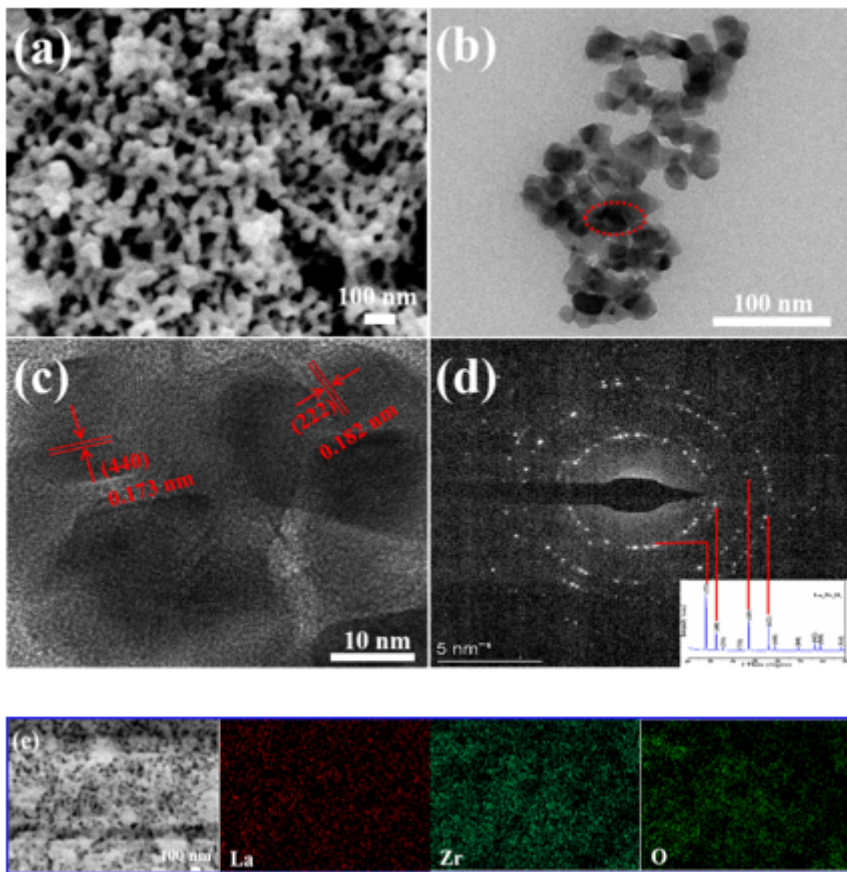


Figure 2

(a) SEM. (b) TEM. (c) HTEM. (d) SAED pattern indexed with XRD peaks and (e) EDS mapping of the as-prepared LZ1.

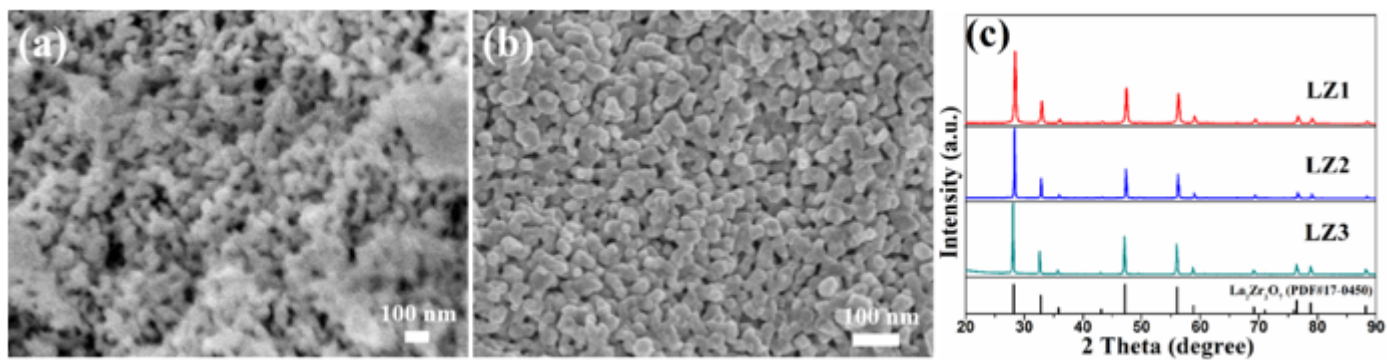


Figure 3

The SEM images of (a) LZ2. (b) LZ3 and (c) corresponding XRD patterns.

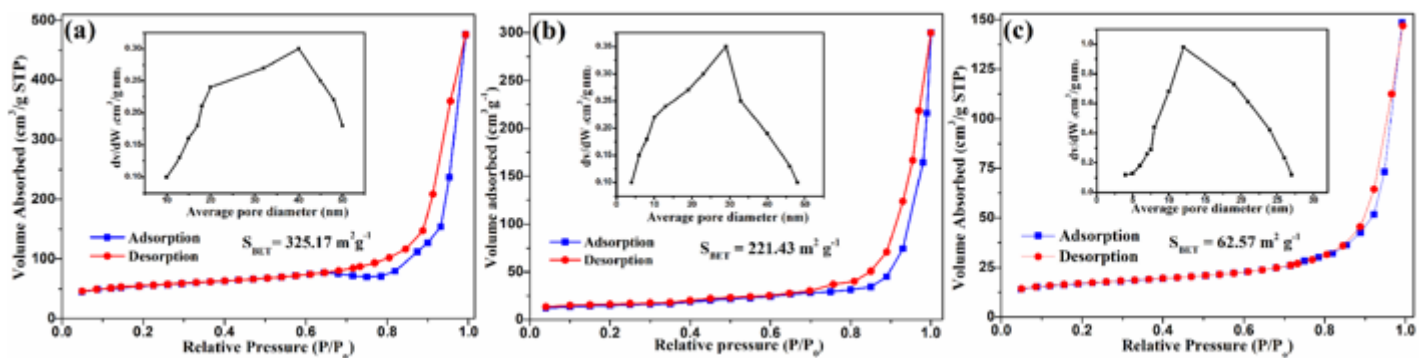


Figure 4

The N₂ adsorption-desorption isotherms and corresponding pore size distributions of sample (a) LZ1. (b) LZ2 and (c) LZ3.

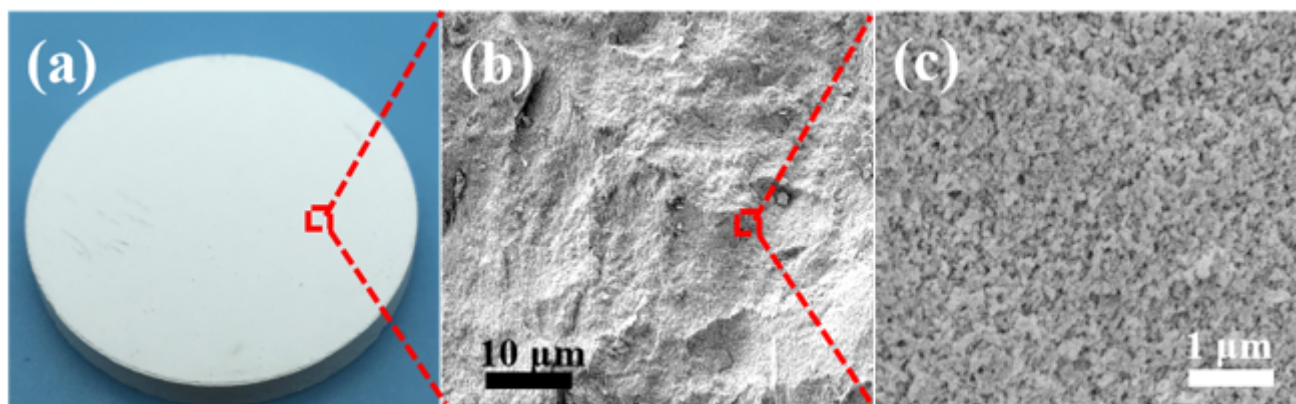


Figure 5

The photograph (a) and microstructures (b), (c) of the representative sample of as-prepared LZ1 bulk with different magnification.

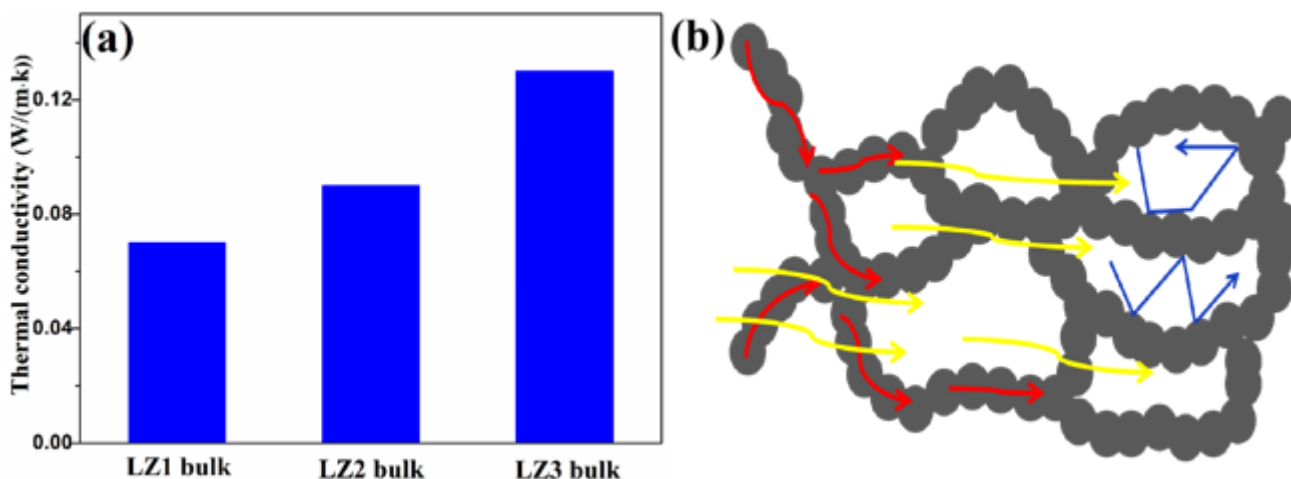


Figure 6

(a) Comparison of room temperature thermal conductivity of the samples. (b) different mechanisms of heat transfer in porous La₂Zr₂O₇ bulk: solid conduction through the particle's chain (red arrows); radiative conduction (yellow arrows); and gaseous thermal conduction (dark blue arrows).

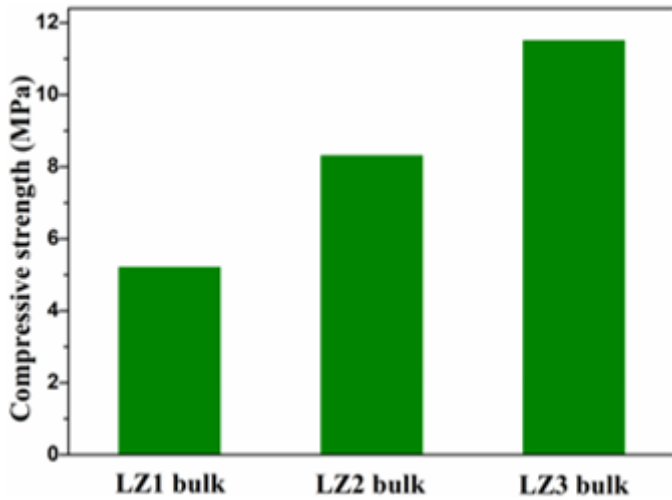


Figure 7

Comparison of compressive strength of the samples.

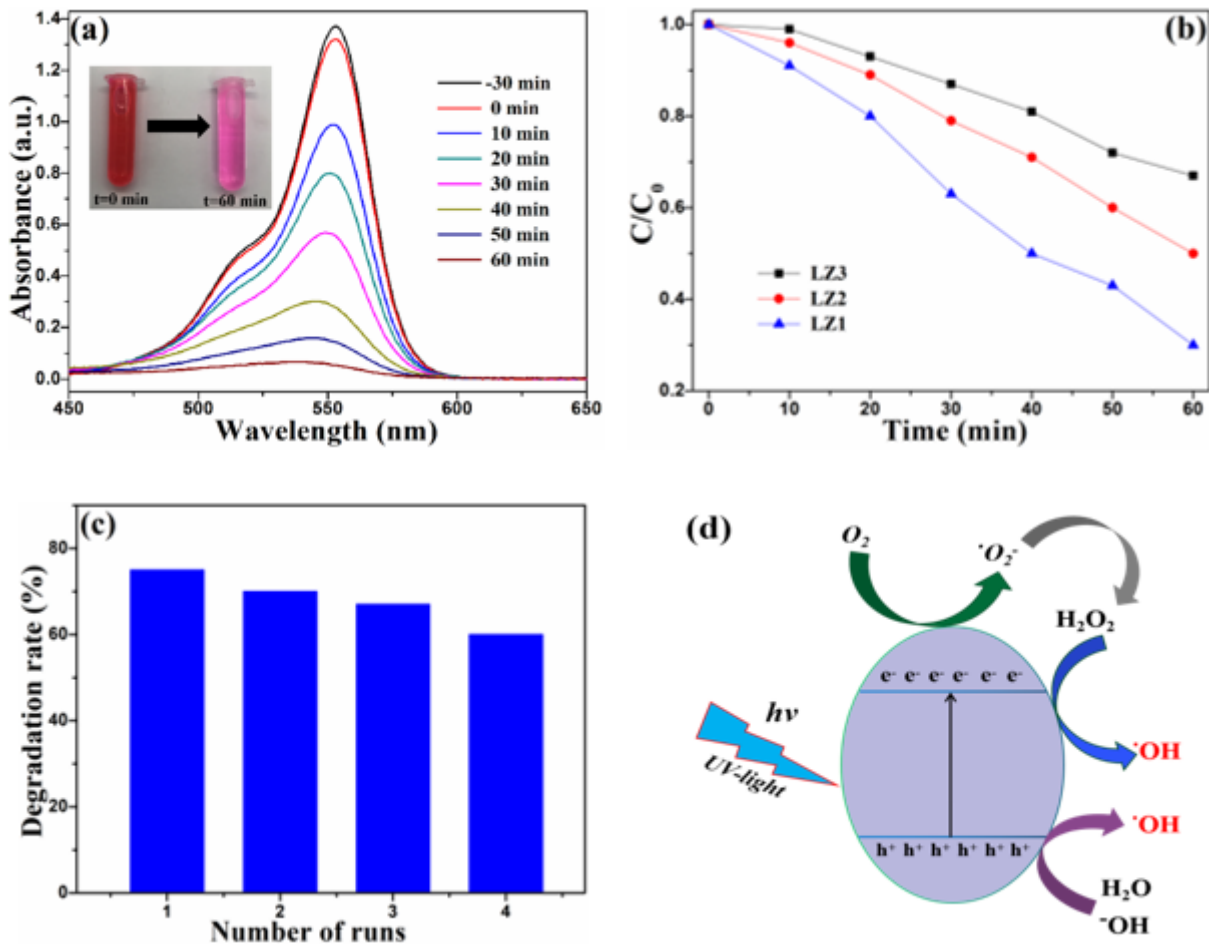


Figure 8

(a) The spectral absorbance of LZ1 for photocatalytic decomposition of RhB with the variation of irradiation time under UV-light. (b) degradation efficiencies curves of RhB as a function of irradiation time. (c) cycling runs for the photodegradation of RhB over LZ1. (d) schematic diagram for the photocatalytic mechanism under UV-light irradiation.

Supplementary Files

This is a list of supplementary files associated with this preprint. Click to download.

- [Scheme1.png](#)